Nanoscale

PAPER

View Article Online
View Journal | View Issue

Cite this: *Nanoscale*, 2023, **15**, 18613

Understanding Yb^{3+}-sensitized photon avalanche in Pr^{3+} co-doped nanocrystals: modelling and optimization†

Magdalena Dudek, *[a] Zuzanna Korczak, [a] Katarzyna Prorok, [a] Oleksii Bezkrovnyi, [a] Lining Sun, [b] Marcin Szalkowski [a,c] and Artur Bednarkiewicz *[a]

Among different upconversion processes where the emitted photon has higher energy than the one absorbed, photon avalanche (PA) is unique, because the luminescence intensity increases by 2–3 orders of magnitude in response to a tiny increase in excitation intensity. Since its discovery in 1979, PA has been observed in bulk materials but until recently, obtaining it at the nanoscale has been a significant challenge. In the present work, the PA phenomenon in β-$NaYF_4$ colloidal nanocrystals co-doped with Pr^{3+} and Yb^{3+} ions was successfully observed at 482 nm ($^3P_0 \rightarrow {}^3H_4$) and 607 nm ($^3P_0 \rightarrow {}^3H_6$) under excitation at 852 nm. The impact of Pr^{3+} ion concentration and pump power dependence on PA behavior was investigated, *i.e.* PA non-linearity slopes of luminescence intensity curves as a function of pump power density as well as PA thresholds. The highest slopes, namely 8.6 and 9.0, and the smallest thresholds equal to 286 kW cm^{-2} and 281 kW cm^{-2}, observed for emission bands at 607 nm and 482 nm, respectively, were obtained for $NaYF_4$:0.5%Pr^{3+},15%Yb^{3+}@$NaYF_4$ colloidal nanocrystals. Besides experimental research, simulations of PA behavior in Pr^{3+}, Yb^{3+} co-doped materials were performed based on differential rate equations describing the phenomena that contribute to the existence of PA. The influence of different processes leading to PA, *e.g.* the rates of nonradiative and radiative transitions as well as energy transfers, on PA performance was simulated aiming to understand their roles in this complex sensitized system.

Received 1st September 2023,
Accepted 30th October 2023

DOI: 10.1039/d3nr04409b

rsc.li/nanoscale

Introduction

Photon avalanche (PA) is a highly non-linear upconversion process during which the luminescence intensity increases rapidly with a minute pump power density increase. In consequence, the characteristic s-shape curve of luminescence intensity (I_L) as a function of pump power density (I_P) is obtained and could be described by the following power law:

$$I_L = I_P^S, \quad (1)$$

where S signifies a slope of the curve and, next to the PA threshold (PA_{TH}) indicating the value above which PA exists, is a characteristic parameter used to describe the PA process. PA was first observed in 1979 by Jay S. Chivian in singly Pr^{3+}-doped $LaCl_3$ and $BaCl_3$ single crystals, with a vision to count medium infrared photons at *ca.* 4.5 mm,[1] which were responsible for the intermediate $^3H_5$ level population and enabled efficient photoexcitation by a green laser source, leading to the $^3H_5 \rightarrow {}^3P_1$ ESA transition. It was predicted that PA nanoparticles may open new possible fields of applications;[2] however, obtaining PA at the nanoscale has been a challenge. All features and characteristics of the PA phenomenon have only recently been clearly and undoubly evidenced in colloidal $NaYF_4$ and $LiYF_4$ nanocrystals doped with Tm^{3+} ions at the nanoscale.[3,4] Since then, the impacts of the local environment,[5] host matrix[6] and light induced photodarkening and recovery in singly Tm^{3+}-doped[7] ions have been studied, and a general multicolor PA emission thanks to the core–shell design and energy migration through a Yb^{3+} (ref. 8) or Gd^{3+} (ref. 9) migration network has been demonstrated. At the nanoscale, PA emission has also been demonstrated in $NaYF_4$ nanocrystals co-doped with Pr^{3+} and Yb^{3+} ions.[8] In the latter case Yb^{3+} ions work as a sensitizer and establish an energy migration network, hosting the migrating PA mechanism (MPA)[8] or sensitized PA (SPA).[10] These studies confirmed the

[a]*Institute of Low Temperature and Structure Research, Polish Academy of Sciences, ul. Okólna 2, 50-422 Wroclaw, Poland. E-mail: a.bednarkiewicz@intibs.pl, m.dudek@intibs.pl*
[b]*Department of Chemistry, College of Sciences, Shanghai University, Shanghai 200444, China*
[c]*Nanophotonics Group, Institute of Physics, Faculty of Physics Astronomy and Informatics, Nicolaus Copernicus University in Toruń, ul. Grudziądzka 5, 87-100 Toruń, Poland*

† Electronic supplementary information (ESI) available. See DOI: https://doi.org/10.1039/d3nr04409b

applicability of the Yb^{3+}, Pr^{3+} PA system for sub-diffraction imaging[8] and luminescence nanothermometry,[10] as predicted previously.[2,11] However, the mechanisms of sensitization of Pr^{3+} avalanche emission by co-doping with Yb^{3+} have to be further studied and clarified.

There are some key conditions required to obtain PA. Firstly, the excitation wavelength has to be resonant with excited state absorption (ESA) and simultaneously far from resonance with ground state absorption (GSA). Additionally, the absorption cross section from the excited state (σ_{ESA}) has to be much higher than from the ground state (σ_{GSA}), which is described as $\beta = \frac{\sigma_{ESA}}{\sigma_{GSA}}$ and should be above 10^4. In order to populate the metastable state, from which ESA can occur, cross-relaxation (CR) processes are necessary. CR relays on the exchange of energy between two ions, one of which is in a higher excited state and the other in a basic energy state. These two ions average their energies and thus produce two ions in an excited, metastable state. Consequently, the population of the metastable level increases in a loop, and absorption occurs more efficiently, which translates into PA emission. The characteristic features of PA are also slow luminescence rise times. Furthermore, to quantify the dynamics of relative changes of the luminescence intensity for the pump power changes, we introduce the parameter D_{AV}, which is the PA luminescence intensity enhancement in response to doubling the excitation power densities, *i.e.*:

$$D_{AV} = \frac{I_L(2 \cdot I_P)}{I_L(I_P)}. \quad (2)$$

The subject of the present work is SPA in β-$NaYF_4$ nanocrystals co-doped with Pr^{3+} and Yb^{3+} ions. Multicolor PA emission at 482 nm ($^3P_0 \rightarrow {}^3H_4$ transition) and 607 nm ($^3P_0 \rightarrow {}^3H_6$ transition) was successfully observed under excitation at 852 nm wavelength in samples co-doped with 15%Yb^{3+} ions and 0.1, 0.3, 0.5 or 0.7% of Pr^{3+} ions. The impacts of the concentration of Pr^{3+} ions and nanocrystal architecture on PA properties have been studied. In particular, the essential parameters describing the avalanching system, like S, PA_{TH}, rise times and D_{AV} were investigated in detail. Additionally, β-$NaYF_4$ nanocrystals singly doped with Pr^{3+}, *i.e.* 0.1%, 0.5%, 1% and 3% ions, were synthesized and investigated, aiming to understand the role of CR and sensitization by Yb^{3+} ions. Moreover, another motivation behind our work was to critically evaluate the origin of red Pr^{3+} emission, as a discrepancy exists in the literature about the energy level (either $^3P_0$ or $^1D_2$) responsible for this transition. Furthermore, simulations of the PA process in Pr^{3+}, Yb^{3+} co-doped crystals were performed. Based on the supposed PA mechanisms and relatively low phonon tetrafluoride materials, differential rate equations (DREs) were rationalized as compared to previous reports. Additionally, we have adopted a 'knock-out'-like approach in DRE modelling, aiming to understand the influence of different individual phenomenological parameters on the PA process, *i.e.* the role of the rates of all the important non-radiative and radiative transitions as well as energy transfers was investigated. This knowledge is essential to further optimize the performance (*e.g.* decrease the PA threshold, increase PA gain or PA slopes) of these avalanching materials for numerous future photonic applications, and likewise to qualitatively understand the generic mechanisms behind sensitization in photon avalanching by other co-dopants.

Results and discussion

The aim of the present work was to understand the origin and mechanism of PA emission of Pr^{3+} ions at the nanoscale. Therefore, a set of β-$NaYF_4$ colloidal nanocrystals singly doped with 0.1%, 0.5%, 1% and 3% of Pr^{3+} ions was synthesized. Additionally, based on earlier reported MPA in Pr^{3+}, Yb^{3+} co-doped β-$NaYF_4$ nanoparticles,[8] a set of samples co-doped with 15% of Yb^{3+} ions in a wide range of concentrations of Pr^{3+} ions, *i.e.* 0.1%, 0.3%, 0.5% and 0.7%, was synthesized. All materials were synthesized by thermal decomposition of lanthanide salts in a core and core–shell architecture. Morphology and structural characterization was carried out for all prepared nanocrystals (Fig. 1 and Fig. S1, S2†). X-ray powder diffraction (XRD) reflexes of the investigated samples are compatible with the XRD pattern of the hexagonal (β) structure of $NaYF_4$ crystals (Fig. 1o and Fig. S2†), which confirms a pure β-$NaYF_4$ phase of the synthesized nanomaterials. The sizes of the nanocrystals were estimated based on transmission electron microscopy (TEM) images. Exemplary TEM pictures and histograms with average dimensions of the synthesized nanocrystals are presented in Fig. 1 and panels (a–l) in Fig. S1.† The diameters of the core nanoparticles are in the range of 16–20 nm and the core–shell dimensions are within 18–31 nm. Most of the crystals feature narrow size distribution, except for core–shell nanocrystals doped with 0.5% of Pr^{3+} ions, where, next to bigger core–shell particles (21 nm), smaller ones (around 10 nm) are observed (Fig. S1b†). We suppose that the shell material, besides crystallization on core nanoparticles, crystallized also as smaller undoped $NaYF_4$ nanocrystals, as we discussed later on the basis of core and core–shell dimensions. An indirect proof of shell deposition is the bigger size of core–shell nanoparticles than that of core nanocrystals. Additionally, undoped shell deposition is directly evidenced by the exemplary energy dispersive X-ray spectroscopy (EDS) map and the profile of Yb^{3+} and Y^{3+} ions prepared for core–shell $NaYF_4$:0.5%Pr^{3+},15%Yb^{3+}@$NaYF_4$ nanocrystals (Fig. 1m and n). The thicknesses of shells were calculated based on the average dimensions of nanocrystals. For most of the spherical core–shell nanoparticles, the shell thickness is around 4 nm (Table 1) with the exception of 0.5%Pr^{3+}-doped ones, which have a shell thickness of around 2 nm (Table S1†). It is evidence that part of the shell material in this sample crystallized as smaller, undoped β-$NaYF_4$ particles. In the case of ellipsoidal core–shell nanocrystals, the shell thickness is around 2 nm in width and between 4 nm and 6 nm in length (Table S1†).

To determine the PA luminescence parameters, the 852 nm wavelength as the excitation one was used,[8] which is resonant

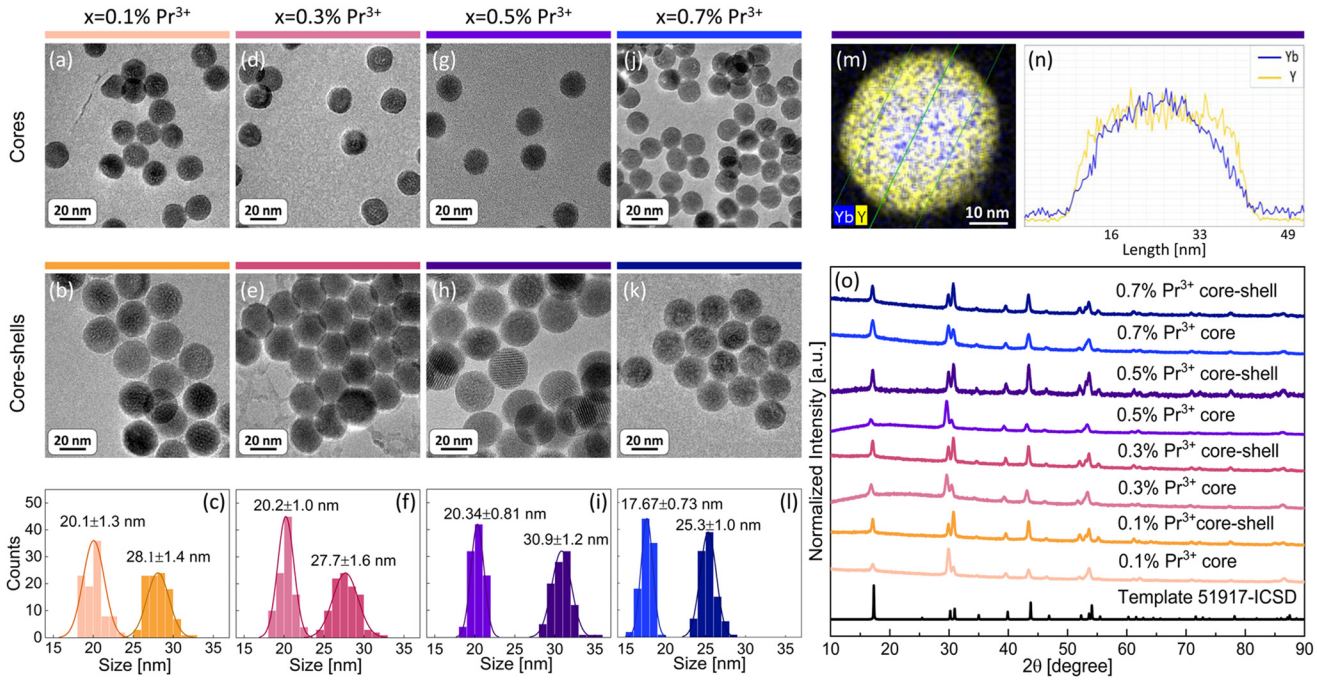

Fig. 1 Characteristic of β-$NaYF_4$ nanocrystals co-doped with *x*%Pr^{3+} and 15%Yb^{3+} ions showing PA: (a, d, g and j) transmission electron microscopy (TEM) images of core nanoparticles; (b, e, h and k) TEM images of core–shell nanocrystals; (c, f, i and l) histograms with average sizes of core and core–shell nanocrystals. (m) Energy dispersive X-ray spectroscopy (EDS) map and (n) EDS profile of Yb^{3+} and Y^{3+} ions in the core–shell $NaYF_4$:0.5% Pr^{3+},15%Yb^{3+}@$NaYF_4$ nanocrystals; (o) X-ray powder diffractions of the β-$NaYF_4$ structure (template) and all the samples.

Table 1 Average dimensions and shell thicknesses of β-$NaYF_4$ nanocrystals co-doped with *x*%Pr^{3+} and 15%Yb^{3+} ions

Dopants *x*% Pr^{3+}, 15%Yb^{3+}	Average core diameter [nm]	Average core–shell diameter [nm]	Average shell thickness [nm]
0.1%Pr^{3+}	20.1 ± 1.3	28.1 ± 1.4	4.0 ± 1.4
0.3%Pr^{3+}	20.2 ± 1.0	27.7 ± 1.6	3.8 ± 1.3
0.5%Pr^{3+}	20.34 ± 0.81	30.9 ± 1.2	5.3 ± 1.0
0.7%Pr^{3+}	17.67 ± 0.73	25.3 ± 1.0	3.80 ± 0.86

with Pr^{3+} ESA ($^1G_4 \rightarrow {}^3P_1$) and simultaneously far from resonance with the GSA of these ions, as is required for PA. Measurements were performed at room temperature (RT). At the beginning, singly Pr^{3+}-doped samples were investigated. The range of ion concentrations was deliberately chosen starting with a very low content, namely 0.1% of Pr^{3+} ions, ending at 3%. It can be expected that a high concentration of ions would lead to the concentration quenching of luminescence intensity. However, even nanocrystals with low Pr^{3+} ion concentrations showed no emission under these excitation conditions (Fig. 2a). The peak at around 725 nm is an artifact resulting from a laser diode and no emission was observed from singly Pr^{3+}-doped nanocrystals. Therefore, nanocrystals co-doped with Pr^{3+} and Yb^{3+} ions were investigated. The 852 nm wavelength can excite Yb^{3+} ions, and then, by energy transfer (ET) processes, the absorbed energy can be further transferred to Pr^{3+} ions. The core and core–shell samples co-doped with 15% Yb^{3+} ions and 0.1%, 0.3%, 0.5% or 0.7% of Pr^{3+} ions successfully showed multicolor emission in the range from 450 nm to 700 nm (Fig. 2b and c). Comparing the emission spectra of the core and core–shell samples, the core–shell nanocrystals feature significantly higher luminescence intensity, confirming the role of the inert passive shell, which protects optically active ions from environment impacts. Furthermore, for the sample singly doped with 0.5%Pr^{3+} ions, no avalanche emission was observed, and the sample co-doped with 0.5%Pr^{3+} and 15%Yb^{3+} ions exhibited multicolor emission, which proves that Yb^{3+} ions play a key role as a sensitizer of PA emission.

The emission bands of the samples co-doped with Pr^{3+} and Yb^{3+} ions were assigned to the following transitions: $^3P_1 \rightarrow {}^3H_4$ (468 nm), $^3P_0 \rightarrow {}^3H_4$ (482 nm), $^3P_1 \rightarrow {}^3H_5$ (522 nm), $^3P_0 \rightarrow {}^3H_5$ (538 nm), $^3P_1 \rightarrow {}^3H_6$ (583 nm), $^3P_0 \rightarrow {}^3H_6$ (607 nm), $^3P_0 \rightarrow {}^3F_2$ (641 nm), $^3P_1 \rightarrow {}^3F_3$ (672 nm), $^3P_1 \rightarrow {}^3F_4$ (693 nm), and $^3P_0 \rightarrow {}^3F_4$ (720 nm) (Fig. 2c). In the literature, the assignment of emission bands in the 580–620 nm range is ambiguous, as in some reports, they are interpreted as emission from the $^3P_1$ level, while others are from the $^1D_2$ level.[8,12–17] Here, as also earlier,[10] we assigned the emission at 607 nm to the $^3P_0 \rightarrow {}^3H_6$ transition. Considering the emission at 607 nm (16 475 cm^{-1}), the energy mismatch is lower for the $^3P_0 \rightarrow {}^3H_6$ transition (ΔE = 16 400 cm^{-1}) than for the $^1D_2 \rightarrow {}^3H_4$ transition (ΔE = 16 800 cm^{-1}). Additionally, to prove that the emission at 607 nm comes from the same level as 482 nm, fluorescence lifetime decay curves for these wavelengths were measured in a wide range of temperatures. Luminescence lifetime curves

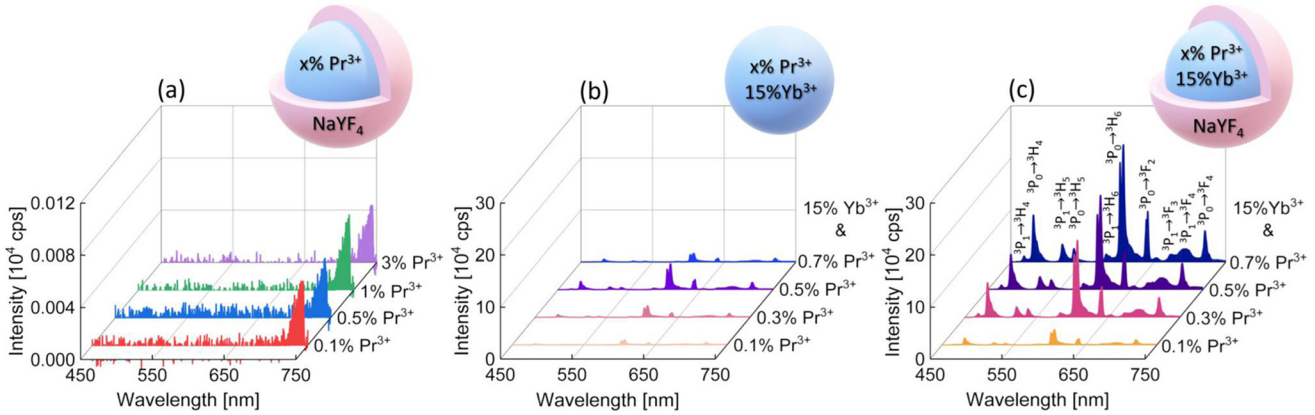

Fig. 2 Anti-Stokes emission spectra of β-$NaYF_4$ nanocrystals: (a) core–shells singly doped with Pr^{3+} ions; (b) cores co-doped with *x*%Pr^{3+}, 15%Yb^{3+}; (c) *x*%Pr^{3+}, 15%Yb^{3+} co-doped cores with a passive shell with assigned transitions. The presented emission spectra were recorded under 852 nm excitation (1.5 MW cm^{-2}) at room temperature.

measured at RT are presented in Fig. S3.† The values of the short and long components of the decay time curves and $\frac{A_1}{A_1 + A_2}$ as a function of temperature are shown in Fig. S4a–d.† The average values of the lifetimes were calculated using the formula:

$$t_{avr} = \frac{A_1 t_1 + A_2 t_2}{A_1 + A_2}, \quad (3)$$

giving 13.6 μs and 17.6 μs for emissions at 607 and 482 nm (both at RT), respectively (Fig. S4a and c†). Measurements of the mentioned luminescence lifetimes helped to confirm that the 607 nm and 482 nm emissions originate from the same level and assign them to 482 nm ($^3P_0 \rightarrow {}^3H_4$) and 607 nm ($^3P_0 \rightarrow {}^3H_6$) transitions. These emission bands, as one of the most intense, were additionally chosen to measure the emission intensity as a function of pump power density. The power density of excitation wavelength increases from 10^4 W cm^{-2} to around 10^7 W cm^{-2} with small (between 1000 and 2000 W cm^{-2}) steps. As a result, characteristic s-shaped curves were obtained (Fig. 3a and b). The pump power dependence measurements were carried out at least two times and the average maximum *S* and average PA_{TH} were calculated (Fig. 3c–f and Table S2†). By comparing the core samples with their

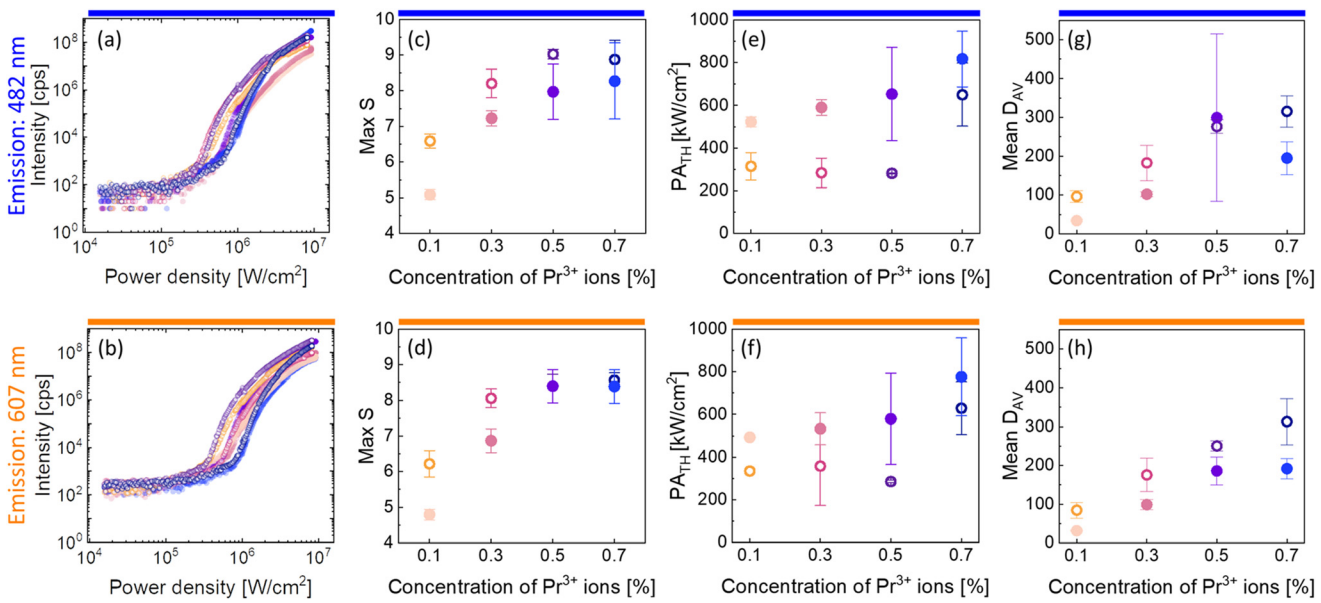

Fig. 3 Characteristic of PA emission in the core and core–shell β-$NaYF_4$ nanocrystals co-doped with 15%Yb^{3+} and 0.1%, 0.3%, 0.5% or 0.7% of Pr^{3+} ions. Subsequent columns: (a and b) pump-power dependence of PA luminescence; (c and d) maximum values of *S*, which are a measure of nonlinearity of the PA process (eqn (1)); (e and f) PA_{TH} pump powers as a function of the concentration of Pr^{3+} ions. (g and h) Mean values of D_{AV} parameters indicating the efficiency of the PA process. These properties were recorded for core (●) and core–shell (○) nanoparticles at 482 nm (top row) and at 607 nm (bottom row). Average values and standard deviations for (c–h) were calculated based on a few (2–4) measurements.

core–shell counterparts, it can be noted that the slope values (Fig. 3c and d) are higher for the core–shell samples, while thresholds (Fig. 3e and f) are lower in their case. Secondly, the inert shell plays an important role in protecting the optically active core from environment impacts, which might result in luminescence quenching. Analyzing Fig. 3c and d, which show the results obtained for various Pr^{3+} doping concentrations, it can be observed that average slope values increase with the amount of Pr^{3+} ions up to 0.5% and then decrease a bit for 0.7%Pr^{3+} ions. For both PA emissions, *i.e.* 482 nm and 607 nm, the biggest average slopes were detected for the core–shell β-$NaYF_4$ nanocrystals co-doped with 15%Yb^{3+}, 0.5%Pr^{3+} ions, which amount to similar values of 9.0 and 8.6, respectively (Table S2†). In the case of thresholds (Fig. 3e and f), for PA emissions at 482 nm and 607 nm, the smallest PA_{TH} values were observed for the core–shell β-$NaYF_4$:15%Yb^{3+},0.5% Pr^{3+}@$NaYF_4$ nanocrystals (281 kW cm^{-2} and 287 kW cm^{-2}, respectively) (Table S2†). Overall, besides Stokes emission lifetime similarity (Fig. S3†), the similarity of the PA behavior at 482 and 607 nm further indicates the same origin of both emission bands, *i.e.* $^3P_0$, and further suggests that no or negligible emission originates from the $^1D_2$ level. This simplifies the description of the sensitized photon avalanche mechanism and has serious implications for further, more detailed analysis and simulations that were carried out. Based on the PA performance, the core–shell 15%Yb^{3+} and 0.5%Pr^{3+} co-doped β-$NaYF_4$ nanocrystals were found to be optimal for PA emission in this investigated set of samples. It is compliant with earlier research.[8] We expect that PA emissions are extremely sensitive to even minor factors responsible for excitation, and therefore the resulting slopes of the pump power dependence curves are not as high as reported from confocal setups. Moreover, one may expect that in core–shell nanoparticle architectures, ion intermixing between the core and shell may occur,[19,20] and thus the actual dopant ion concentration may be slightly diluted there. In consequence, optimal conditions for PA emission may become diminished, leading to reduced nonlinearity and an increased PA threshold. However, regardless of the exact values of S nonlinearity, we draw general conclusions and observe and discuss trends in order to instruct further development of PA nanomaterials as well as clarify the mechanism of PA sensitization.

There were calculated D_{AV} values (Fig. 3g and h), which, according to eqn (2), describe how much the luminescence intensity increases upon doubling the power density. The core–shell nanocrystals turned out to be more sensitive to the changes and the most sensitive was the β-$NaYF_4$:15%Yb^{3+},0.7%Pr^{3+}@$NaYF_4$ sample. Another characteristic PA feature is the slowing down of the emission rise time for power densities close to the threshold. Here, parameters $\tau_{50\%}$ and $\tau_{80\%}$ were adopted to describe the time needed to obtain 50% and 80% of maximum luminescence intensity (at an infinitely long excitation time), respectively. The average values of $\tau_{50\%}$ and $\tau_{80\%}$ are presented in Fig. S5.† The highest values of rise times were observed for β-$NaYF_4$:15% Yb^{3+},0.1%Pr^{3+}@$NaYF_4$ nanocrystals.

To understand the PA mechanism, besides experimental investigations, simulations of the PA process in the Pr^{3+}, Yb^{3+} co-doped system and in singly Pr^{3+}-doped nanocrystals were performed. Compared with earlier studies,[8] here a significantly simpler energy diagram of the Pr^{3+}, Yb^{3+} system was adopted for modeling. The supposed PA mechanism in the Pr^{3+}, Yb^{3+} ion co-doped system is demonstrated in Fig. 4a and, excluding gray elements, was used to write DREs (eqn (S1)–(S7)†). The correspondence of the properties measured at 607 and 482 nm indicates that the emissions come from the same level and therefore the $^1D_2$ level can be excluded from analysis. This feature allowed us to rationalize the rate equation model as compared to earlier studies, perform the next computational studies in a more effective way and draw general and more clear conclusions about the origin of PA in the PrYb system studied here. As expected, the 852 nm wavelength, thanks to its resonance with the ESA [$^1G_4 \rightarrow {}^3P_1$] transition in Pr^{3+} ions as well as its incompatibility with the GSA of Pr^{3+} (Fig. 4a), turned out to be appropriate for PA. Absorption cross sections from the ground and excited states in Pr^{3+} were indicated in modeling as σ_{ESA} and σ_{GSA}, respectively. As was experimentally evidenced, the Yb^{3+} ions are necessary for the existence of PA. Thus, the absorption cross section in Yb^{3+} was also taken into consideration (σ_{Yb}).

The metastable level (starting with ESA) should be initially populated to provide efficient ESA. Here, three energy transfer processes populating the metastable $^1G_4$ level in Pr^{3+} ions were considered. First, CR between Pr^{3+} ions [$^3P_1$, $^3H_4$] → [$^1G_4$, $^1G_4$] (W_{CR1}), second, w_{65} indicating energy transfer upconversion (ETU) from Pr^{3+} to Yb^{3+} ions [Yb^{3+}: $^2F_{7/2}$, Pr^{3+}: $^3P_1$] → [Yb^{3+}: $^2F_{5/2}$, Pr^{3+}: $^1G_4$] and finally, w_{71} energy transfer (ET) from Yb^{3+} to Pr^{3+} ions [Yb^{3+}: $^2F_{5/2}$, Pr^{3+}: $^3H_4$] → [Yb^{3+}: $^2F_{7/2}$, Pr^{3+}: $^1G_4$]. These ETU and ET were also considered as energy transfer processes going in opposite directions and indicated as w_{74} and w_{64}, respectively. Additionally, CR populating the $^3H_5$ level in Pr^{3+} ions (W_{CR2}) was considered. This process was the basis for obtaining PA in Pr^{3+} for the first time by Jay S. Chivian,[1] therefore, it should not be overlooked in the first approximation, despite the fact that the ESA occurs from $^1G_4$ and not $^3H_5$. Consequently, radiative and nonradiative emission processes from $^3H_6$ and $^3H_5$ levels were taken into consideration, namely τ_3, τ_2, NR_{32} and NR_{21}. Other two nonradiative processes, *i.e.* NR_{54} and NR_{43}, were also considered. Because both PA emissions (482 nm and 607 nm) originate from the same $^3P_0$ level, we could disregard the $^1D_2$ level from further analysis and thus simplify the description of the phenomenological energy transfer DRE model and speed up the data simulation presented in Fig. 4. Simultaneously, emissions from $^3P_1$ are weaker compared with emissions from $^3P_0$ (Fig. 2c). This is because of a small energy break between levels $^3P_1$ and $^3P_0$ (<600 cm^{-1}), which can be easily bridged by matrix phonons (energy of one phonon in $NaYF_4$ ~350 cm^{-1}). Thus, in the modeling, the $^3P_1$ level has been disregarded. Emission bands from $^3P_0$, $^1G_4$ and Yb^{3+} ions were characterized by lifetimes at these levels: τ_5, τ_4 and τ_{Yb}, respectively. Based on the supposed PA mechanism and analyzing the emission spectra of PA nanocrystals, the processes illustrated as gray in Fig. 4a have been omitted from the modeling. Finally, the DRE (eqn (S1)–(S7)†) model was designed to evaluate and qualitatively understand the PA

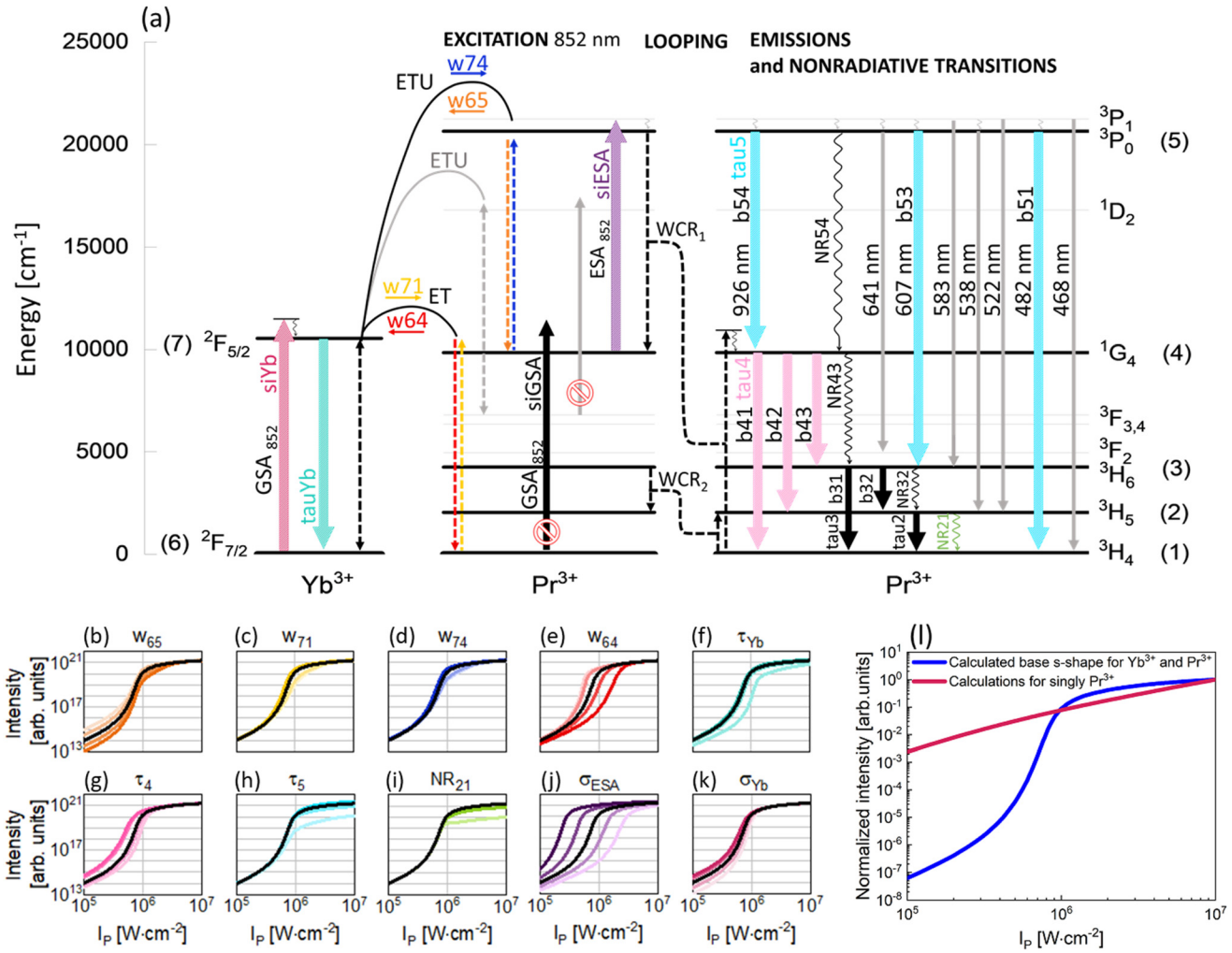

Fig. 4 The mechanism and susceptibility of Yb^{3+}-sensitized Pr^{3+} photon avalanching to the processes involved in the SPA phenomenon: (a) energy diagram and the PA mechanism of the Pr^{3+}, Yb^{3+} co-doped system. This graph, excluding the gray elements, has been used to define the DREs. Panels from (b) to (k) contain simulated s-shaped dependences of luminescence intensity as a function of pump power density depending on the values of particular parameters involved in the SPA, namely nonradiative transitions (w_{65}, w_{71}, w_{74}, w_{64}, NR_{21}), radiative lifetimes (τ_{Yb}, τ_4, τ_5) and absorption cross sections (σ_{ESA}, σ_{Yb}), used in the developed model. Individual panels show how the variation of these parameters (one at a time) affects the s-shape profiles. Saturated and desaturated colors correspond to the increase or decrease of a given parameter value, respectively, while s-shapes obtained for pristine (literature) values are black. (l) Pump power-dependent Pr^{3+} PA luminescence intensity profiles obtained from theoretical modeling (navy blue for Yb^{3+}, Pr^{3+} and pink for pure Pr^{3+}-doped systems). The impact of the Yb^{3+} sensitizer on PA emission characteristics is evaluated by modeling, *i.e.* the Yb^{3+}, Pr^{3+} co-doped system exhibits PA emission, while the singly Pr^{3+}-doped system shows conventional upconversion.

phenomenon and its susceptibility to other material properties. The parameters utilized to solve the DREs were mostly adopted from the literature on $LiYF_4$ matrix-based luminescent materials and are summarized in Table S3.† The rates of nonradiative transition were estimated on the basis of the chart of probabilities of nonradiative transitions of Ln^{3+} ions in a tetragonal $LiYF_4$ laser crystal as a function of energy gap at $T = 0$.[21] The probability of nonradiative transitions from the starting level, J, to the end level, J', is described as $W_{JJ'}$ (eqn (S9)†). These calculations are presented in the ESI.†

The prepared DREs were resolved and the characteristic s-shape curve illustrating luminescence intensity as a function of pump power density was obtained, which is presented in Fig. 4 in all small panels (b–k) as a black curve. All the other color s-shaped curves indicate how the increase (more intense color) or decrease (paler shade) of individual parameters influences the features of PA, what will be discussed later. It is important to notice that the prepared DREs were resolved also for the singly Pr^{3+}-doped system (*i.e.* by zeroing all processes describing Yb^{3+} and Pr^{3+} interactions, namely w_{74}, w_{65}, w_{71}, w_{64} and σ_{Yb}). The model excluding Yb^{3+} ions (Fig. 4l) clearly showed that singly Pr^{3+} ions under 852 nm excitation are not sufficient to obtain PA emission, and energy transfer processes between the two selected ions play a key role.

The original DREs (eqn (S1)–(S7))† were then used to experimentally evaluate how the individual parameters influence the features of PA. To understand their roles, the values of these individual parameters of DREs were artificially and purposefully increased and decreased around the literature values. The changes were not uniform for each of the parameters, but particular parameters were tuned individually, and specific values are presented in Table S4.† The results obtained from these calculations are presented in Fig. 4(b–k) and Fig. S6.† Not all parameters affect PA in a significant way, thus, only those parameters that substantially influence the shape of the pump power dependence or slope are presented here. Although W_{CR1} seems to be the key process for PA performance, it does not influence PA features, because there exist other more intense processes that populate the metastable $^1G_4$ level. The Pr^{3+} concentration is low, thus CR processes, including W_{CR2}, are not efficient enough to power the avalanching. Here, w_{65} plays a role of CR and populates the $^1G_4$ metastable level, which is necessary for ESA.[22] Moreover, the value of w_{65} is higher than that of W_{CR1}, which supports the hypothesis that Yb^{3+}, not W_{CR1}, is responsible for PA. Yb^{3+} ions not only support avalanching, but are also essential components of the system, which enables PA emission in this configuration. To obtain PA in a single Pr^{3+}-doped material, there will be necessary excitation conditions used by Chivian.[1] An increase of w_{65} enables more efficient ESA, which causes a steeper slope and shifts the PA_{TH} to higher values (Fig. 4b and Fig. S6a†). Similarly to w_{65}, w_{71} populates the $^1G_4$ level of Pr^{3+} ions and for more intense w_{71}, the slopes are higher (Fig. S6b†). The w_{74} process could be assigned to ESA and its higher values increase slopes (Fig. S6c†). The w_{64} transfers energy from Pr^{3+} to Yb^{3+} ions, picking up the energy from the metastable state. The greater the share of w_{64}, the more difficult it is to achieve PA (Fig. 4e) and the slope decreases (Fig. S6d†). However, w_{64} pumps Yb^{3+}, which is necessary for PA, but Yb^{3+} can get entangled in energy migration to the surface. It is widely known that Yb^{3+} ions are very susceptible to surface quenching by the overtones of water vibrations (3300 cm^{-1}); therefore, surface effects also have a vital impact. Thus, the role of Yb^{3+} is twofold. First, Yb^{3+} enables PA, but facilitates quenching on the surface, which may not be prevented by a passive shell even for the thicknesses studied here. Decreasing the radiative lifetime of Yb^{3+} ions (τ_{Yb}), for example, due to surface quenching, increases PA_{TH} by up to one order of magnitude (Fig. 4f). Also, the saturation of the curve is smoother. The shorter lifetime of Yb^{3+} ions may indicate that w_{64} and w_{65} processes are more intense and consequently PA_{TH} also increases. Let us consider the other radiative lifetimes. First, the τ_4, which is a radiative lifetime of the $^1G_4$ metastable level, is considered. A longer τ_4 facilitates the more efficient occurrence of ESA. Consequently, PA_{TH} is lower (Fig. 4g) but also slopes decrease (Fig. S6f†). For τ_5, only minute variation was observed (Fig. S6g†). In the cases of τ_2 and τ_3, insignificant changes have been observed. These lifetimes determine the population of levels (2) and (3), which are necessary for cross-relaxation described by W_{CR2}. These processes will be critical for excitation based on the $^3H_5 \rightarrow {}^3P_1$ transition applied by Jay S. Chivian, but here, under 852 nm photoexcitation wavelength, are not significant. If these lifetimes were very long, respective levels could store electrons and reduce the ground state population, thus hindering the CR processes. But here, their impact is negligible, which in turn suggests that the ET between Yb^{3+} and Pr^{3+} is more important than the CR within the Pr^{3+} ion couples. The lifetimes considered here are radiative, thus nonradiative transitions were additionally taken into account in the model. Here, to make the model easier, some Pr^{3+} levels were overlooked and NR_{54} and NR_{43} were adopted to describe nonradiative transitions between levels $^3P_0 \rightarrow {}^1G_4$ (10 800 cm^{-1}) and $^1G_4 \rightarrow {}^3H_4$ (9850 cm^{-1}), respectively. The energy gaps of these transitions are wide; therefore the probabilities of the processes are not high. However, it is important to remember that under experimental conditions, these transitions could be more efficient than how they appear in the numerical considerations. Calculations for increased and decreased NR_{54} and NR_{43} were performed, but no clear differences in the s-shape were observed for values up to three orders of magnitude smaller or larger than the original values. The other two nonradiative processes are closely connected with W_{CR2} and here do not change too much; however the impact of NR_{21} was observed (Fig. 4i and Fig. S6h†), indicating the importance of having Pr^{3+} ions in the ground state to initiate PA emission.

Ending the description of modeling, let's come back to the key conditions necessary to obtain PA emission. One of these conditions is a significantly high value of cross section for absorption from the excited state and a simultaneously negligible cross section for absorption from the ground state. The 852 nm excitation wavelength fulfills these conditions. As expected, σ_{GSA} has not influenced the features of PA, while σ_{ESA} has the biggest impact on the PA_{TH} values. Higher values of σ_{ESA} facilitate PA, shifting the PA_{TH} to smaller values, and conversely, lower values of σ_{ESA} increase the threshold value (Fig. 4j). Moreover, the slopes increase for bigger σ_{ESA} (Fig. S6f†). It confirms that ESA plays a key role in being necessary in the PA process and higher values of σ_{ESA} positively influence PA. In the case of σ_{Yb}, the changes are negligible. A decrease of the parameter impedes PA by moving PA_{TH} to higher power densities (Fig. 4k); however, the slopes increase (Fig. S6j†). Yb^{3+} ions take part in two processes populating $^1G_4$. For w_{65}, Yb^{3+} ions in the ground state are required, while for w_{71}, Yb^{3+} ions in the excited state are necessary. From these two processes, w_{65} is found to be more intense; therefore, in this case Yb^{3+} ions in the ground state could help to increase a slope.

Besides PA measurements, basic spectroscopy studies of the synthesized samples has been carried out, including measurements of the absorption, emission and excitation spectra as well as luminescence lifetimes. These results are presented in the ESI.† In all cases, the amounts of the investigated samples were the same to enable a quantitative comparison. Considering the samples co-doped with Pr^{3+} and Yb^{3+} ions, where the amount of Yb^{3+} ions was constant (15%), one can see that it is reflected in the absorption spectra (Fig. S7a†)

because the absorption values coming from Yb^{3+} ions are at the same level. Simultaneously, the absorption of Pr^{3+} ions increases with an increase of Pr^{3+} amount, as illustrated in the inset of Fig. S7a†. A similar situation is observed in the case of singly Pr^{3+}-doped $NaYF_4$ nanocrystals, where absorption also increases with Pr^{3+} ion concentration (inset in Fig. S7b†). Insets were prepared based on the integral area of the peak at 444 nm corresponding to the $^3H_4 \rightarrow {}^3P_2$ transition. Excitation spectra (Fig. S8a and S8c†) were recorded for the samples co-doped with Pr^{3+}, Yb^{3+} ions and singly Pr^{3+} doped, by monitoring emission at 980 nm and 607 nm, respectively. In all cases the most intensive peaks were obtained at 444 nm. For the core–shell nanocrystals co-doped with Pr^{3+} and Yb^{3+} ions, the integral area under the peak at 444 nm decreases with an increasing concentration of Pr^{3+} ions (Fig. S8a†). It means that the absorbed energy is less effectively transferred to Yb^{3+} ions when the Pr^{3+} concentration is higher, which is due to the increased concentration quenching between neighboring Pr^{3+} ions (*i.e.* increasing Pr^{3+} concentration from 0.1 to 0.7% quenched the emission intensity by *ca.* 2 fold). It is astonishing to see that the concentration quenching is not that strong in singly Pr^{3+}-doped samples, as the integral area under the peak at the same wavelength (444 nm, monitoring Pr^{3+} emission at 607 nm) initially increases with Pr^{3+} ion concentration up to 1%, and then decreases slowly by *ca.*30% for samples doped with 1 and 8% Pr^{3+}. This can only be explained by the larger amounts of lanthanides (>10%), the cooping of large[23] and small ions, *i.e.* 1.179 Å and 1.042 Å Pr^{3+} and Yb^{3+} ions, respectively, for 9-fold coordination positions and/or the role of Yb^{3+} ions, which most probably cluster dopants more effectively than for dopant levels of 1%. It is well known that low concentrations of optically active ions minimize luminescence quenching relative to high dopants. However, the arrangement of atoms in the lattice is also important. It is worth mentioning here studies on nanocrystals with orthorhombic crystallographic structures, in which lanthanide ions were arranged in tetrahedral arrays.[24] Such an arrangement of ions resulted in minimizing the migration of excitation energy to defects by preserving the excitation energy within the sublattice domain. The lack of control over the organization of nanomaterials at the atomic scale is one of the reasons limiting their optical performance. Providing control over the mixing of cations at the core–shell interface can provide a dramatic improvement in quantum efficiency.[18]

Considering that the most intense peak in the absorption spectra was obtained at 444 nm, emission spectra (Fig. S8b and d†) were recorded under excitation at 444 nm and multicolor emission was observed. Insets for emission spectra were prepared on the basis of the integral area under the peak at 482 nm assigned to the $^3P_0 \rightarrow {}^3H_4$ emission. For small amounts of Pr^{3+} ions, namely 0.1%, 0.3%, 0.5%, and 0.7%, the emission intensity increased with the concentration of Pr^{3+} ions (inset in Fig. S8b†). Moreover, the core–shell samples, where the inert shell protects optically active ions from the environment, have shown more intense luminescence in comparison with the cores, as was expected. In the case of singly Pr^{3+}-doped samples, where the range of concentrations of Pr^{3+} ions was wider (from 0.1% to 8%), initially the luminescence intensity increases with the concentration of Pr^{3+} ions up to the sample doped with 3% of Pr^{3+}. Subsequently, for samples doped with 5% and 8% of Pr^{3+} ions, the luminescence intensity decreases. It is connected with the concentration quenching effect, which occurs for highly doped nanocrystals.

Experimental

Materials and methods

β-$NaYF_4$ nanocrystals doped with praseodymium as well as co-doped with praseodymium and ytterbium ions were synthesised. The selected crystal matrix is appropriate for the PA phenomenon due to its low phonon energy. Additionally, compared with a cubic α-$NaYF_4$ structure, a hexagonal one is brighter. All nanocrystals were prepared in a core and core-undoped shell architecture.

Synthesis methods

Reagents. All chemical reagents were used without any further purification. Yttrium oxide Y_2O_3 (99.99%), praseodymium oxide Pr_6O_{11} (99.99%), ytterbium oxide Yb_2O_3 (99.99%) and trifluoroacetic acid (99%) were purchased from Alfa Aesar. Acetic acid (99.5%), sodium hydroxide NaOH (≥98.0%), methanol (99.8%), ethanol (96%), *n*-hexane (czda) and chloroform (98.5%) were purchased from POCH S.A. Ammonium fluoride NH_4F (≥98.0%), sodium trifluoroacetate (98%), octadecene (90%) and oleic acid (90%) were purchased from Sigma-Aldrich.

Preparation of the precursor in the form of lanthanide acetates. Stoichiometric amounts of lanthanide oxides, namely Y_2O_3, Yb_2O_3 and Pr_6O_{11} (2.5 mmol), were mixed in acetic acid and water (volume ratio 1 : 1) in a Teflon vessel. The prepared mixture was kept at 200 °C for 60 minutes to form acetates. The final precursor was obtained by evaporation of residual acetic acid and water using a rotary evaporator in a pre-vacuum (<8 hPa) and drying at 140 °C for 12 hours.

Preparation of the precursor in the form of lanthanide trifluoroacetates. A stoichiometric amount of Y_2O_3 (2.5 mmol) was dissolved in a solution of water (10 mL) and trifluoroacetic acid (10 mL) and kept at 90 °C for one hour to form yttrium trifluoroacetates. The final precursor was prepared by evaporation of residual trifluoroacetic acid and water using a rotary evaporator and drying at 140 °C for 12 hours.

Synthesis of core β-$NaYF_4$:*x*%Pr^{3+} and β-$NaYF_4$:*x*%Pr^{3+},15% Yb^{3+} nanoparticles. The core nanoparticles were synthesized by the thermal decomposition of oleate salts in high boiling solvents, based on the procedure described earlier by Abel *et al.*[25] First, a precursor in the form of lanthanide acetates was prepared as described above. In a typical synthesis, oleic acid (30 mL) and 1-octadecene (75 mL) were added to a flask with the precursor. The solution was stirred and heated to 140 °C under vacuum in order to remove residual oxygen and water. Under such conditions, the mixture was kept for 30 minutes. Subsequently, the solution was cooled down to

around 70 °C under a nitrogen atmosphere and a mixture of NaOH (12 mmol) and NH_4F (20 mmol) in 13 mL of methanol was added. Then, the solution was stirred for 10 minutes at 60 °C. Subsequently, the temperature was increased to 80 °C and the solution was maintained under these conditions for 45 minutes to slowly evaporate methanol. Then, the mixture was heated up to 110 °C and kept under vacuum for 15 minutes. After removing methanol, the reaction temperature was quickly increased to 300 °C and the synthesis spanned for one hour under a nitrogen atmosphere. Then, the solution was cooled down to around 80 °C and the nanoparticles were precipitated by the addition of ethanol and centrifugation at 10 000 rpm for 10 minutes. After that, the prepared nanocrystals were dispersed in a minimal amount of *n*-hexane and again precipitated with ethanol at 14 000 rpm for 10 minutes. The resulting nanoparticles were dispersed in 10 mL of chloroform.

Ellipsoidal shell deposition. Nanocrystals with an inert ellipsoidal shell were prepared by the thermal decomposition of oleate salts. At the beginning a precursor in the form of lanthanide acetates from Y_2O_3 (2.5 mmol) was prepared as described earlier. The next steps were analogous to the core synthesis. Oleic acid (30 mL) and octadecene (75 mL) were added to the round-bottomed flask containing the precursor. The solution was heated up to 140 °C and kept under vacuum for half an hour. Subsequently, the mixture was cooled down to around 60 °C under a nitrogen atmosphere and a solution of NH_4F (12 mmol) and NaOH (20 mmol) in 13 mL of methanol was added to the flask. The dilution was heated up to 80 °C and the flask was opened for 45 minutes to slowly evaporate methanol. The temperature was then increased to 110 °C and the solution was kept under vacuum for 15 minutes. Then, the solution was cooled down to 60 °C and the earlier prepared core nanocrystals dispersed in chloroform were added to the flask under a nitrogen atmosphere. Then, chloroform was evaporated. Afterwards, the mixture was heated up to 300 °C and kept under a nitrogen atmosphere for one hour. After synthesis, the solution was cooled down to about 80 °C and ethanol was added to precipitate the nanoparticles. The nanocrystals were separated by centrifugation at 10 000 rpm for 10 minutes. Afterwards, the nanoparticles were washed with *n*-hexane, once more precipitated with ethanol, centrifuged at 14 000 rpm for 10 minutes and finally dispersed in chloroform (10 mL).

Spherical shell deposition. Nanoparticles with a spherical shell were prepared by the thermal decomposition of trifluoroacetates. At the beginning a precursor in the form of trifluoroacetates was prepared, as described above. Afterwards, sodium trifluoroacetate (5 mmol), oleic acid (40 mL) and 1-octadecene (40 mL) were placed in a round-bottomed flask containing the precursor. Subsequently, the solution was maintained under vacuum at 120 °C for half one hour to remove residual oxygen and water. Afterwards, the mixture was cooled down to 60 °C under a nitrogen atmosphere, the core nanocrystals (5 mL) were added to the flask and the mixture was stirred for 10 minutes. Then, chloroform was evaporated. At the beginning the temperature was increased up to 80 °C and the flask was opened for 30 minutes, and subsequently, the temperature was increased up to 110 °C and the solution was kept under vacuum for 15 minutes. Afterwards, the solution was quickly heated up to 300 °C and maintained under a nitrogen atmosphere for one hour. After that, the solution was cooled down to 80 °C and the nanocrystals were precipitated by the addition of ethanol and centrifuged at 10 000 rpm for 10 minutes. Then, the precipitated nanoparticles were dispersed in *n*-hexane and once more precipitated with ethanol and then centrifuged at 14 000 rpm for 10 minutes. Finally, the nanocrystals were dispersed in chloroform (5 mL).

Setup description and the methodology of PA measurements. The photoexcitation power density dependence of luminescence intensity was investigated and measurements of the PA rise times were performed on a custom-built optical microscopy system. The range in which the pump power density laser can be measured is 10^2–10^7 W cm^{-2}. The sample was excited with a single mode laser diode (FPL852S – 852 nm, 350 mW), producing an 852 nm beam. The outgoing laser beam passes through a set of gray filters of different densities that attenuate the light, so the power density of the excitation light can be precisely controlled without spectral tuning. Then, a dichroic mirror (DMSP805R) reflects the excitation beam to the side (left) port of an inverted microscope (Nikon Ti-2 Eclipse). Furthermore, the laser beam was focused by the objective lens (Nikon Plan Apo 40×, NA = 0.95, W.D = 0.21 mm) on a sample placed on a microscope cover slip (Menzel-Glaser, 24 × 60 mm). The sample's emission was collected by the objective lens and it exited through the left port of the microscope and then passed through the dichroic mirror (DMSP805R), where it could be simultaneously recorded using two PMT detectors (1001M and 2101M from Thorlabs) connected to a four-channel photon counter (quTAG). The luminescent light of the sample was separated by a dichroic mirror (DMSP505R), and then selected in front of the detectors by bandpass filters (F01-475 – Semrock and 600BP – Omega Optical). Thus, it is possible to record luminescence intensities by two channels at 480 nm and 610 nm, simultaneously. The obtained experimental data were analyzed using our home-developed Matlab code, which is described in the following point. Using an Andor Shamrock i500 spectrograph equipped with a Newton CCD camera (DU920P-BEX2-DD), emission spectra were recorded. The absorption spectra shown in Fig. S7† were recorded using a Cary 5000 UV-Vis-NIR spectrophotometer (Agilent Technologies). Excitation and emission spectra as well as lifetimes were collected with a FLS1000 (Edinburgh Instruments).

Calculations of *S* and PA_{TH} values. *S* and PA_{TH} values were determined using our home-developed Matlab code, which is available in our web repository (**https://github.com/LuNASIanalysis/Photon-Avalanche-PA-**). Our algorithm was based on the fitting of the linear function to the logarithm from the raw data (which is analogous to fitting the exponential function to raw data) point by point. For each of the points, the fit covers the maximal range of the surrounding data, which fulfils the given certainty. Such an approach allowed us to reduce the impact of the noise on the determined *S* values. The highest *S* values which were obtained for

the analyzed dataset were selected for presentation. Similarly, the PA_{TH} values were determined as the power corresponding to the cross-section point of the lines tangent to the logarithm of the raw data for the pre-avalanche region and tangent to the logarithm of the raw data in the range of maximum S values. The s-shaped curves were measured few times (2–4) and based on them, the average S, PA_{TH} and D_{AV} values together with the standard deviation were determined.

Conclusions

In summary, SPA emission at 482 nm ($^3P_0 \rightarrow {}^3H_4$) and 607 nm ($^3P_0 \rightarrow {}^3H_6$) under excitation at 852 nm in β-$NaYF_4$ colloidal nanocrystals co-doped with 15%Yb^{3+} and a small (0.1 to 0.7%) amount of Pr^{3+} ions was successfully observed and studied. We have clearly demonstrated the critical role of undoped shell passivation in the PA emission characteristics, which is obviously beneficial and diminishes the impact of the local chemical environment (quenchers, solvent) on both the emitting (Pr^{3+}) and sensitizing–migrating (Yb^{3+}) ions. Under the same experimental conditions no emission from singly Pr^{3+} ion-doped β-$NaYF_4$ nanocrystals was observed under 852 nm photoexcitation. It emphasizes the key role of Yb^{3+} ions, which are necessary to obtain PA emission under chosen experimental conditions. During experimental investigations, the highest S of 8.6 and 9.0 as well as the smallest PA_{TH} of 286 kW cm^{-2} and 281 kW cm^{-2} were observed for the core–shell sample co-doped with 15%Yb^{3+} and 0.5%Pr^{3+} ions for emissions at 607 nm and 482 nm, respectively. Therefore, the optimal sample composition for SPA $NaYF_4$:0.5%Pr^{3+},15%Yb^{3+}@$NaYF_4$ was confirmed.[8] Both Stokes emission and photon avalanche emission let us clearly confirm that the $^1D_2$ level does not take part in energy transfer, and thus can be excluded, unlike in some other existing reports, from the analysis. In consequence, elimination of processes related to $^1D_2$ level this let us simplify the phenomenological set of rate equations and ultimately enablws to simulate the behavior, mechanism and performance of the sensitized photon avalanche emission, indicating the critical role of the Yb^{3+} sensitizer in this system under 852 nm photoexcitation. Moreover, the simulations of SPA allowed us to understand the impact of energy transfer parameters on PA features. These calculations confirmed that PA emissions from Pr^{3+} ions under excitation at 852 nm are possible only with the assistance of Yb^{3+} ions; thus, crystals singly doped with Pr^{3+} ions do not exhibit PA features at such a photoexcitation wavelength. The obtained experimental and theoretical results have shown and allowed us to understand the important role of Yb^{3+} ions, which are necessary to obtain PA emission from Pr^{3+} ions under excitation at 852 nm.

Author contributions

MD: conceptualization, synthesis, data curation, data analysis, investigation, visualization, and writing the original draft; ZK: data analysis, investigation, visualization, and writing – review & editing; KP: data analysis and writing – review & editing; OB: investigation and data analysis; LS: writing – review & editing; MS: investigation, methodology, software, and writing – review & editing; AB: conceptualization, funding acquisition, methodology, software, project administration, resources, supervision, validation, writing the original draft, review and editing.

Conflicts of interest

There are no conflicts to declare.

Acknowledgements

This research was funded in whole or in part by the following projects 2018/31/B/ST5/01827 (M. D., Z. K., M. S., A. B.) and 2021/43/B/ST5/01244 (A. B.). K. P. acknowledges the financial support from NCN, Poland, grant number 2018/31/D/ST5/01328. Calculations have been carried out using the resources provided by the Wroclaw Centre for Networking and Supercomputing (**https://wcss.pl**), grant no. 529.

References

1 J. S. Chivian, W. E. Case and D. D. Eden, *Appl. Phys. Lett.*, 1979, **35**, 124–125.
2 A. Bednarkiewicz, E. M. Chan, A. Kotulska, L. Marciniak and K. Prorok, *Nanoscale Horiz.*, 2019, **4**, 881–889.
3 C. Lee, E. Xu, Y. Liu, A. Teitelboim, K. Yao, A. Fernandez-Bravo, A. Kotulska, S. H. Nam, Y. D. Suh, A. Bednarkiewicz, B. E. Cohen, E. M. Chan and P. J. Schuck, *Nature*, 2021, **589**, 230–235.
4 M. Dudek, M. Szalkowski, M. Misiak, M. Ćwierzona, A. Skripka, Z. Korczak, D. Piątkowski, P. Woźniak, R. Lisiecki, P. Goldner, S. Maćkowski, E. M. Chan, P. J. Schuck and A. Bednarkiewicz, *Adv. Opt. Mater.*, 2022, 2201052.
5 K. W. C. Kwock, C. Lee, A. Teitelboim, Y. Liu, K. Yao, S. B. Alam, B. E. Cohen, E. M. Chan and P. J. Schuck, *J. Phys. Chem. C*, 2021, **125**, 23976–23982.
6 Z. Zhang, A. Skripka, J. C. Dahl, C. Dun, J. J. Urban, D. Jaque, P. J. Schuck, B. E. Cohen and E. M. Chan, *Angew. Chem., Int. Ed.*, 2023, **62**, e202212549.
7 C. Lee, E. Z. Xu, K. W. C. Kwock, A. Teitelboim, Y. Liu, H. S. Park, B. Ursprung, M. E. Ziffer, Y. Karube, N. Fardian-Melamed, C. C. S. Pedroso, J. Kim, S. D. Pritzl, S. H. Nam, T. Lohmueller, J. S. Owen, P. Ercius, Y. D. Suh, B. E. Cohen, E. M. Chan and P. J. Schuck, *Nature*, 2023, **618**, 951–958.
8 Y. Liang, Z. Zhu, S. Qiao, S. Qiao, X. Guo, R. Pu, H. Tang, H. Liu, H. Dong, T. Peng, L.-D. Sun, J. Widengren and Q. Zhan, *Nat. Nanotechnol.*, 2022, **2022**, 1–7.
9 A. Skripka, M. Lee, X. Qi, J.-A. Pan, H. Yang, C. Lee, P. J. Schuck, B. E. Cohen, D. Jaque and E. M. Chan, *Nano Lett.*, 2023, **23**, 7100–7106.

10 Z. Korczak, M. Dudek, M. Majak, M. Misiak, Ł. Marciniak, M. Szalkowski and A. Bednarkiewicz, *Low Temp. Phys.*, 2023, **49**, 322–329.
11 M. Szalkowski, M. Dudek, Z. Korczak, C. Lee, Ł. Marciniak, E. M. Chan, P. J. Schuck and A. Bednarkiewicz, *Opt. Mater.: X*, 2021, **12**, 100102.
12 M. F. Joubert, *Opt. Mater.*, 1999, **11**, 181–203.
13 P. Boutinaud, R. Mahiou, N. Martin and M. Malinowski, *J. Lumin.*, 1997, **72–74**, 809–811.
14 S. Kuck, A. Diening, E. Heumann, E. Mix, T. Sandrock, K. Sebald and G. Huber, *J. Alloys Compd.*, 2000, **300–301**, 65–70.
15 S. Hao, W. Shao, H. Qiu, Y. Shang, R. Fan, X. Guo, L. Zhao, G. Chen and C. Yang, *RSC Adv.*, 2014, **4**, 56302–56306.
16 M. Y. Tsang, P. Fałat, M. A. Antoniak, R. Ziniuk, S. J. Zelewski, M. Samoć, M. Nyk, J. Qu, T. Y. Ohulchanskyy and D. Wawrzyńczyk, *Nanoscale*, 2022, **14**, 14770–14778.
17 H. Liang, S. Zhang and C. Li, *J. Phys. Chem. C*, 2013, **117**, 2216–2221.
18 F. A. Cardona, N. Jain, R. Popescu, D. Busko, E. Madirov, B. A. Arús, D. Gerthsen, A. De Backer, S. Bals, O. T. Bruns, A. Chmyrov, S. Van Aert, B. S. Richards and D. Hudry, *Nat. Commun.*, 2023, **14**, 4462.
19 D. Hudry, I. A. Howard, R. Popescu, D. Gerthsen and B. S. Richards, *Adv. Mater.*, 2019, **31**, 1900623.
20 D. Hudry, A. De Backer, R. Popescu, D. Busko, I. A. Howard, S. Bals, Y. Zhang, A. Pedrazo-Tardajos, S. Van Aert, D. Gerthsen, T. Altantzis and B. S. Richards, *Small*, 2021, **17**, 2104441.
21 A. A. Kaminskii, *Crystlline Lasers: Physical Processes and Operating Schemes*, 1996.
22 V. Lupei, *Spectrochim. Acta, Part A*, 1998, **54**, 1615–1632.
23 R. D. Shannon, *Acta Crystallogr., Sect. A: Cryst. Phys., Diffr., Theor. Gen. Crystallogr.*, 1976, **32**, 751–767.
24 J. Wang, R. Deng, M. A. MacDonald, B. Chen, J. Yuan, F. Wang, D. Chi, T. S. A. Hor, P. Zhang, G. Liu, Y. Han and X. Liu, *Nat. Mater.*, 2014, **13**, 157–162.
25 K. A. Abel, J. C. Boyer and F. C. J. M. van Veggel, *J. Am. Chem. Soc.*, 2009, **131**, 14644–14645.